



14TH CANADIAN MASONRY SYMPOSIUM
MONTREAL, CANADA
MAY 16TH – MAY 20TH, 2021



ADVANCED 3D INTERFACE MODEL FOR FINITE ELEMENT ANALYSIS OF UNREINFORCED MASONRY STRUCTURES

Zeng, Bowen¹ and Li, Yong²

ABSTRACT

Detailed finite element modeling of masonry structures is essential to understand their complex mechanical behavior accounting for different failure mechanisms, which highly depends on the mortar joints (i.e., mortar layer and unit-mortar interaction). As such, this study presents a plasticity-based constitutive model for a 3D interface element that is capable of capturing various failure modes of mortar joints, including tension cracking, shear sliding, and compressive crushing. It is characterized by two hyperbolic yield surface criteria: tension-shear failure surface and compressive cap surface. The evolutions of the yield surfaces and state variables are formulated based on the concept of strain-softening/hardening. A fully implicit Euler Backward integration algorithm, combined with a local-global Newton-Raphson (NR) solver, is adopted to achieve the predictor-corrector returning mapping procedure in the numerical formulation. Additionally, the variations of dilatancy and fracture energy are introduced, aiming to describe the mechanical behavior of mortar joints accurately. The model is implemented in the finite element software Abaqus via UMAT. The proposed interface model is validated with the unit-mortar-unit assemblages and unreinforced masonry walls. The capability of newly developed interface model shows its potential to be used to further explore the mechanical behavior of masonry structures.

KEYWORDS: *finite element modeling, interface element, implicit integration algorithm, masonry structures*

¹ Ph.D. Student, Department of Civil and Environmental Engineering, University of Alberta, Edmonton, AB, Canada., bzeng1@ualberta.ca

² Assistant Professor, Department of Civil and Environmental Engineering, University of Alberta, Edmonton, AB, Canada., yong9@ualberta.ca

INTRODUCTION

Masonry structures have been widely used throughout the world due to its durability, strength hydro-thermal performance, and aesthetics. The mechanical behavior of masonry structures depends on the properties of the masonry constituents and their interaction. Due to the heterogeneity and anisotropy of masonry composites, simulation or prediction of structural masonry behavior remains a challenging task. Detailed finite element modeling (referred to as micro modeling), characterized by the explicit modeling of each constituent and interface, has been proved to be a robust tool to study the masonry structure. Although at high computational cost, micro modeling allows capturing all the possible failure modes. To achieve a compromise between computational cost and accuracy, the simplified micro modeling approach was proposed in [1]. In this approach, mortar joints and unit-mortar contacts are lumped into interfaces while units are modeled with size expansion to keep the masonry structures' overall geometry.

As the key aspect of the simplified micro modeling approach, the interface model should be able to consider all possible failure modes: tension cracking, shear sliding, and compressive crushing. Great efforts have been devoted to developing interface models. For example, Lourenco made an early attempt to develop a multi-yield surface model [1], which had later been extensively used and refined by other researchers [2] [3]. However, most current constitutive models were implemented in the 2D space. Also, some important characteristics were not well considered in the formulation, such as: the variation of dilatancy and fracture energy. As evidenced by the experimental results [4], the dilatancy effects will decrease with the increase of normal compressive stress and plastic shear displacement. Inappropriate descriptions of the dilatancy model may increase normal stress, resulting in a considerable overestimate of shear capacity in the pressure-dependent model. For the fracture energy, it can be observed that the higher compressive stress will improve the ductility and energy dissipation capacity [4], inducing a larger value for mode II fracture energy, which should also be considered in the model formulation.

As such, this paper presents a new 3D multi-yield surface model for interface element, which can be used in the finite element analysis of masonry structure to capture all known possible interfacial failure modes. The proposed multi-yield surface interface model is characterized by two hyperbolic yield surface criteria, which can overcome the numerical singularity in the tension-shear region. The dilatancy effects and the variation of fracture energy are incorporated into the proposed interface model to describe the mortar joint behavior more accurately. A fully implicit Euler Backward integration algorithm, combined with a local-global Newton-Raphson (NR) solver, is adopted to achieve the predictor-corrector returning mapping procedure in the numerical formulation. The auto-adaptive sub-stepping algorithm is used to enhance the accuracy, robustness, and efficiency. Finally, unit-mortar-unit assemblages and masonry walls are simulated to validate the proposed interface model.

INTERFACE CONSTITUTIVE MODEL FORMULATION

The proposed interface model is characterized by the traction-separation relationship. The interfacial behavior in the elastic regime can be written in the matrix form shown in Equation 1:

$$\begin{bmatrix} \sigma_n \\ \tau_s \\ \tau_t \end{bmatrix} = \mathbf{K} \mathbf{d} \mathbf{u} = \begin{bmatrix} k_{nn} & & \\ & k_{ss} & \\ & & k_{tt} \end{bmatrix} \begin{bmatrix} \delta_n \\ \delta_s \\ \delta_t \end{bmatrix} \quad (1)$$

where three stiffness constants k_{nn} , k_{ss} and k_{tt} relate the stress components (i.e., σ_n , σ_s , σ_t) and the displacement separations (i.e., δ_n , δ_s , δ_t) in the normal and tangential directions of the interface.

Multi-yield surface criterion

The proposed multi-yield surface criterion consists of two hyperbolic surfaces: tension-shear failure surface (f_1) and compressive cap surface (f_2), shown in Figure 1. Compared with the Mohr-Coulomb and tension cut-off yield criterion commonly used in the masonry interface model [1], the proposed model, which is described by a continuous and differentiable tension-shear yield function, can overcome the computational singularity in the non-smooth corner of the tension-shear region. Two yield criteria are adopted for the tension-shear yield surface f_1 and the compression cap failure surface f_2 , as given in Equation 2 and Equation 3, respectively:

$$f_1 = -(c - \sigma_n \tan \varphi) + \sqrt{\tau_s^2 + \tau_t^2 + (c - \sigma_t \tan \varphi)^2} \quad (2)$$

$$f_2 = -(f_c + \sigma_n \tan \theta) + \sqrt{\tau_s^2 + \tau_t^2 + (f_c - \sigma_c \tan \theta)^2} \quad (3)$$

where c , σ_t , $\tan \varphi$ are the cohesion, tensile strength, and the frictional coefficient (i.e., tangent of frictional angle φ), respectively; f_c , σ_c , $\tan \theta$ are the peak compressive strength, compressive strength, asymptote slope of compression cap, respectively.

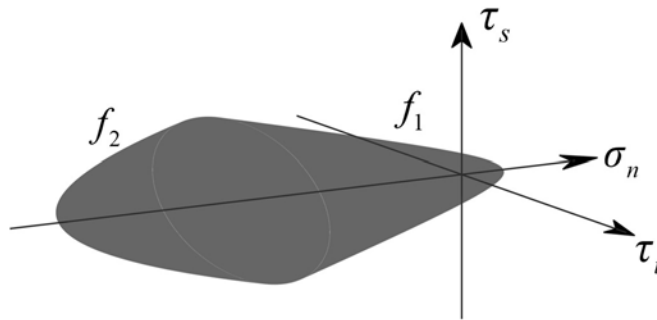


Figure 1: Yield surface in the 3D space

Flow direction

Similar to some frictional materials (e.g., soil, rock, concrete), masonry's mortar joints also exhibit the 'dilatancy' phenomenon [4] under shear loading, accompanied by the volume increase and shear resistance buildup. Accordingly, in the tension-shear failure region, a non-associated flow

rule is adopted to determine the displacement flow direction. The plastic potential g_1 is formulated as Equation 4:

$$g_1 = -(c_q - \sigma_n \tan \psi) + \sqrt{\tau_s^2 + \tau_t^2 + (c_q - \sigma_t \tan \psi)^2} \quad (4)$$

where c_q is the apparent cohesion, $\tan \psi$ is the tangent of dilatancy angle, referred as ‘dilatancy coefficient’, σ_t is the tensile strength. In contrast, for the compression cap yield surface f_2 , the associated flow rule is assumed.

State variables evolution

When at least one yield criterion is violated, the yield surface(s) will shrink or expand based on the strain-softening/hardening law. In the tension-shear failure region, the evolution of tensile strength σ_t and cohesion c , originally proposed in [1], are used here:

$$\sigma_t = f_t \exp\left(-\frac{f_t \kappa_1}{G_I}\right), \quad c = c_0 \exp\left(-\frac{c_0 \kappa_2}{G_{II}}\right) \quad (5)$$

where f_t is the peak tensile strength, G_I is the mode I fracture energy, c_0 is the peak cohesion strength, G_{II} is the mode II fracture energy, κ_1 and κ_2 are two softening scalars, formulated in the rate form, given in Equation 6:

$$\dot{\kappa}_1 = \sqrt{\langle \dot{u}_n^p \rangle^2 + \left(\frac{G_I}{G_{II}} \times \frac{c_0}{f_t} \sqrt{(\dot{u}_s^p)^2 + (\dot{u}_t^p)^2}\right)^2}, \quad \dot{\kappa}_2 = \sqrt{\left(\frac{G_{II}}{G_I} \times \frac{f_t}{c_0} \langle \dot{u}_n^p \rangle\right)^2 + (\dot{u}_s^p)^2 + (\dot{u}_t^p)^2} \quad (6)$$

where u_n^p , u_s^p and u_t^p are the plastic displacements in the normal, first tangential, and second tangential direction, respectively. The Macaulay bracket $\langle \rangle$ means that a compressive stress state has no contribution to the plastic deformation in the normal direction. The quadratic combinations of plastic displacements in Equation 6 ensure that the loss percentages for tensile strength and cohesion are equal through the entire softening process. This fully coupled tension-shear softening model is consistent with the fact that both softening behaviors are related to the interface debonding at the micro-level [1].

Similar to the cohesion strength loss, the frictional coefficient $\tan \phi$ has a gradual change during the plastic deformation process. The evolution of frictional coefficient is coupled with cohesion softening, given in Equation 7:

$$\tan \phi = \tan \phi_0 + \frac{c - c_0}{c_0} (\tan \phi_0 - \tan \phi_r) \quad (7)$$

where $\tan \phi_0$ and $\tan \phi_r$ are the initial and residual frictional coefficients, respectively.

The fracture energy represents the ductility and energy dissipation capacity of mortar joints. Thus, the correct formulation of the fracture energy is necessary in the constitutive model. Previous experimental research showed the dependence of mode II fracture energy G_{II} on the compressive normal stress. A comprehensive regression analysis indicated that a linear relationship between mode II fracture energy G_{II} and compressive normal stress σ_n can be as the general tendency [4], given by Equation 8:

$$G_{II} = \begin{cases} a\sigma_n + G_{II}^0 & \sigma_n < 0 \quad \text{under compression} \\ G_{II}^0 & \sigma_n \geq 0 \quad \text{under tension} \end{cases} \quad (8)$$

where a is a negative constant parameter, G_{II}^0 is the fracture energy when $\sigma_n=0$.

For the plastic potential surface g_1 , apparent cohesion c_q and dilatancy coefficient $\tan\psi$ need to be defined. The evolution law of apparent cohesion c_q is the same with cohesion c as shown in Equation 5 with a different initial value c_q^0 . For the dilatancy coefficient, as evidenced by the experimental results [4], it will decrease with increasing plastic shear displacement; furthermore, the dilatancy effect is very limited under the high compressive normal stress. Consequently, an exponential decay term related to resultant plastic shear displacement and a linear pressure dependence relationship, originally proposed in [2], are extended to three-dimensional space, shown in Equation 9:

$$\tan\psi = \begin{cases} \tan\psi_r + (\tan\psi_0 - \tan\psi_r) e^{-\delta\sqrt{(u_s^p)^2 + (u_t^p)^2}} & \sigma_n \geq 0 \\ \tan\psi_r + (\tan\psi_0 - \tan\psi_r) \left(1 - \frac{\sigma_n}{\sigma_u}\right) e^{-\delta\sqrt{(u_s^p)^2 + (u_t^p)^2}} & \sigma_u \leq \sigma_n < 0 \\ 0 & \sigma_n < \sigma_u \end{cases} \quad (9)$$

where $\tan\psi_0$ is the dilatancy coefficient when $\sigma_n=0$ and $u_s^p=u_t^p=0$, $\tan\psi_r$ is the residual dilatancy coefficient, δ is the dilatancy softening scalar, σ_u is the compressive stress at which $\tan\psi=0$, referred to as ‘critical dilatancy compressive stress’ in this study.

Regarding the variables in the compression cap yield surface, the hardening/softening law for compressive strength σ_c was taken from [1], as shown in Equation 10:

$$\sigma_c = \begin{cases} \bar{\sigma}_i + (\bar{\sigma}_p - \bar{\sigma}_i) \sqrt{\frac{2\kappa_3 - \kappa_3^2}{\kappa_p} - \frac{\kappa_3^2}{\kappa_p^2}} & 0 \leq \kappa_3 < \kappa_p \\ \bar{\sigma}_p + (\bar{\sigma}_m - \bar{\sigma}_p) \left(\frac{\kappa_3 - \kappa_p}{\kappa_m - \kappa_p} \right)^2 & \kappa_p \leq \kappa_3 < \kappa_m \\ \bar{\sigma}_r + (\bar{\sigma}_m - \bar{\sigma}_r) e^{\frac{2\bar{\sigma}_m - \bar{\sigma}_p}{\kappa_m - \kappa_p} \frac{\kappa_3 - \kappa_m}{\bar{\sigma}_m - \bar{\sigma}_r}} & \kappa_3 > \kappa_m \end{cases} \quad (10)$$

where $\bar{\sigma}$ and κ with subscripts i , m , p and r denote the initial, medium, peak and residual values in terms of compressive strength σ_c and softening/hardening scalar κ_3 . f_c is the peak compressive strength (i.e., $f_c = \bar{\sigma}_p$), the softening/hardening scalar κ_3 is defined as the quadratic combinations of three plastic displacement components in the rate form, as shown in Equation 11:

$$\dot{\kappa}_3 = \sqrt{(\dot{u}_n^p)^2 + (\dot{u}_s^p)^2 + (\dot{u}_t^p)^2} \quad (11)$$

PLASTICITY INTEGRATION ALGORITHM

Auto-adaptive sub-stepping algorithm

In the context of sub-stepping strategy, a single load step with a displacement increment \mathbf{du} is discretized into several sub-steps, resulting in a sub-incremental displacement $\omega_i \mathbf{du}$ ($0 < \omega_i < 1$) in each sub-step, given in Equation 12:

$$\mathbf{du} = \sum \mathbf{du}_i = \sum \omega_i \mathbf{du} \quad \text{and} \quad \sum \omega_i = 1 \quad (12)$$

where ω_i is the sub-step reduction factor. An auto-adaptive step size control strategy, proposed in [5], is used to adjust the reduction factor, which helps to minimize the computational cost:

$$\frac{\omega_{i+1}}{\omega_i} = \left(\frac{Tol}{error} \right)^{1/x} \quad (13)$$

where Tol is the prescribed tolerance, $error$ is the residual which is updated in each NR iteration, and x is a constant value to influence the sub-step size change ratio. It is worth mentioning that x should be well defined to avoid a large variation in sub-step size, which may result in the numerical instability.

Multi-yield surface plasticity integration strategy

Generally, the specific case in which both yield criteria introduced in Equations (1) and (2) are satisfied is discussed here. The non-smooth corner is defined by the intersection region of the tension-shear yield surface and compression cap as shown in Figure 1. According to the multi-yield surface plasticity strategy proposed by Simo [6], in the presence of yielding, the plastic strain

increment is obtained as a linear combination of the plastic strain rates of the two yield surfaces, given in Equation 14:

$$d\mathbf{u}^p = \dot{\lambda}_1 \frac{\partial \mathbf{g}_1}{\partial \boldsymbol{\sigma}_{n+1}} + \dot{\lambda}_2 \frac{\partial \mathbf{g}_2}{\partial \boldsymbol{\sigma}_{n+1}} \quad (14)$$

where $d\mathbf{u}^p = [du_n^p, du_s^p, du_t^p]^T$ is the plastic displacement vector, $\dot{\lambda}_1$ and $\dot{\lambda}_2$ are the plastic multipliers.

Subsequently, for each sub-step, the predictor-corrector returning mapping strategy based on the Euler Backward algorithm gives a set of nonlinear equations in Equation 15:

$$\begin{cases} \boldsymbol{\sigma}_{i+1} - \boldsymbol{\sigma}_i - \omega_{i+1} \mathbf{K} d\mathbf{u} + \dot{\lambda}_{1,i+1} \mathbf{K} \frac{\partial \mathbf{g}_1}{\partial \boldsymbol{\sigma}_{i+1}} + \dot{\lambda}_{2,i+1} \mathbf{K} \frac{\partial \mathbf{g}_2}{\partial \boldsymbol{\sigma}_{i+1}} = \mathbf{0} \\ \boldsymbol{\kappa}_{i+1} - \boldsymbol{\kappa}_i + \Delta \boldsymbol{\kappa}_{i+1} = \mathbf{0} \\ \mathbf{f}(\boldsymbol{\sigma}_{i+1}, \boldsymbol{\kappa}_{i+1}) = \mathbf{0} \end{cases} \quad (15)$$

where subscript $i+1$ represents the sub-step level. The unknowns in the nonlinear Equation 15 are $\boldsymbol{\sigma}_{i+1}$, $\boldsymbol{\kappa}_{i+1}$, and $\dot{\lambda}_{i+1}$. A standard NR method is adopted to solve the nonlinear system to ensure the quadratic convergence provided that the initial solution sufficiently close to the exact one. The residuals of Equation 15 can be linearized as shown in Equation 16:

$$\mathbf{r}(\boldsymbol{\sigma}_{i+1}^{k+1}, \boldsymbol{\kappa}_{i+1}^{k+1}, \dot{\lambda}_{i+1}^{k+1}) = \mathbf{r}(\boldsymbol{\sigma}_{i+1}^k, \boldsymbol{\kappa}_{i+1}^k, \dot{\lambda}_{i+1}^k) + \mathbf{J}(\boldsymbol{\sigma}_{i+1}^k, \boldsymbol{\kappa}_{i+1}^k, \dot{\lambda}_{i+1}^k) \begin{bmatrix} d\boldsymbol{\sigma}_{i+1}^{k+1} & d\boldsymbol{\kappa}_{i+1}^{k+1} & d\dot{\lambda}_{i+1}^{k+1} \end{bmatrix}^T \quad (16)$$

where \mathbf{r} represents the residual for each NR iteration, \mathbf{J} is the Jacobian matrix; the NR iteration cycles are indicated by the superscripts k and $k+1$. The exact solution can be obtained by letting the LHS of residual be equal to 0. The results can be improved iteratively by Equation 16 until the residual reaches a prescribed tolerance.

For the global NR iteration at the structural level, the consistent tangent operator, defined as $\frac{\partial \boldsymbol{\sigma}}{\partial d\mathbf{u}}$, is needed for the current load step to achieve the quadratic convergence. $\frac{\partial \boldsymbol{\sigma}}{\partial d\mathbf{u}}$ can be computed by differentiating the Equation 15 with respect to $d\mathbf{u}$ and applying the chain rule, leading to Equation 17:

$$\mathbf{J}(\boldsymbol{\sigma}_{i+1}, \boldsymbol{\kappa}_{i+1}, \dot{\lambda}_{i+1}) \begin{bmatrix} \frac{\partial \boldsymbol{\sigma}_{i+1}}{\partial d\mathbf{u}} & \frac{\partial \boldsymbol{\kappa}_{i+1}}{\partial d\mathbf{u}} & \frac{\partial \dot{\lambda}_{i+1}}{\partial d\mathbf{u}} \end{bmatrix}^T = \begin{bmatrix} \frac{\partial \boldsymbol{\sigma}_i}{\partial d\mathbf{u}} + \omega_{i+1} \mathbf{K} & \frac{\partial \boldsymbol{\kappa}_i}{\partial d\mathbf{u}} & \mathbf{0} \end{bmatrix}^T \quad (17)$$

The recursive structure in Equation 17 means that the consistent tangent operator from the previous sub-step has to be considered for the current sub-step update. The final solution for $\frac{\partial \boldsymbol{\sigma}}{\partial d\mathbf{u}}$ will be obtained until the summation of sub increments is equal to the total displacement increments. The initial conditions for Equation 17 are corresponding to the case $i=0$, shown in Equation 18:

$$\frac{\partial \sigma_{i+1}^0}{\partial du} = \mathbf{0}, \frac{\partial \kappa_{i+1}^0}{\partial du} = \mathbf{0} \quad (18)$$

FINITE ELEMENT MODEL VALIDATION

The proposed constitutive model for interface element is implemented in the commercial Finite Element Package Abaqus via the user-defined subroutine UMAT [7] and then validated by two models at different scales: unit-mortar-unit assemblages and masonry walls.

Unit-mortar-unit assemblages

Different test arrangements of unit-mortar-unit assemblage were discussed in [4]. Two representative experimental series under compression-shear loading, referred to as ‘CS-brick90’ and ‘CS-block96’ [4], are simulated here.

For the material parameters used in the FE simulation, the elastic stiffness constants were determined as a relatively large value to best fit the curves in Figure 2. For the plastic tension and shear material properties, all the parameters are determined directly from the experimental report [4]. The adopted material parameters of interface element are provided in Table 1, only elastic behavior is considered for the units.

Table 1: Material parameters for the interface [4]

Specimen	Tension		Shear					
	f_t (MPa)	G_I (N/mm)	c_0 (MPa)	c_q^0 (MPa)	G_{II}^0 (N/mm)	a	$\tan\phi_0$	$\tan\phi_r$
CS-brick90	0.42	0.0011	1.1	$100 c_0$	0.02	-0.14	0.82	0.85
CS-block96	0.02	0.0005	0.14	$100 c_0$	0.005	-0.02	0.75	0.73

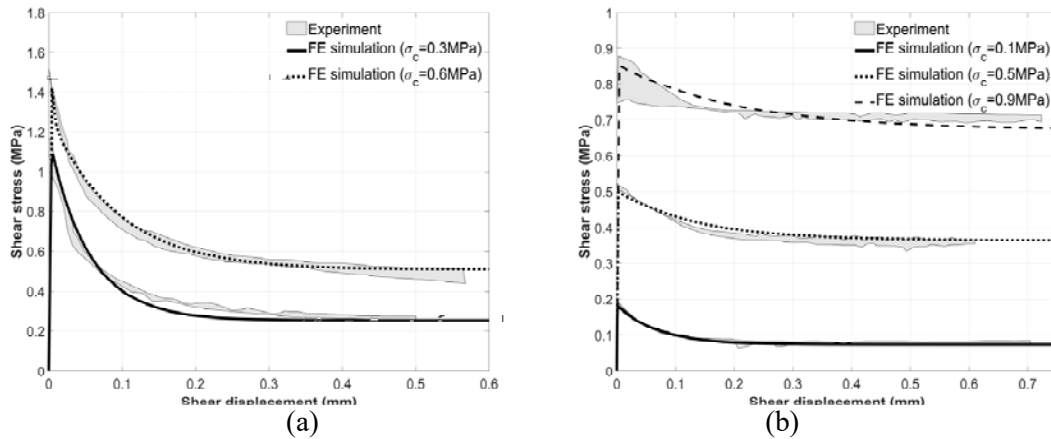


Figure 2: Comparison between numerical and experimental results for unit-mortar-unit assemblages under compression-shear loading: (a) CS-brick90; (b) CS-block96

The simulated shear stress-displacement curves are compared with the experimental ones, as shown in Figure 2. It can be observed that a good agreement with the experimental results is achieved in terms of the peak strengths and post peak behaviors.

Another unit-mortar-unit assemblage in direct shear [8] was simulated to validate the dilatancy behavior. The dilatancy behavior is illustrated by the relationship of normal plastic displacement u_n^p and resultant shear plastic displacement:

$$u_\tau^p = \sqrt{(u_s^p)^2 + (u_t^p)^2} \quad (18)$$

Similarly, the strength-related parameters were obtained directly from the experimental report [8]. For the dilatancy-related material parameters, the two critical dilatancy coefficients (i.e., $\tan\varphi_0$ and $\tan\varphi_r$) are determined as the slopes of $u_n^p - u_\tau^p$ curve when $u_\tau^p=0$ and u_τ^p is large enough such that the dilatancy coefficient reaches a stable residual value. Dilatancy softening scalar δ is calibrated to match the dilatancy softening trend (i.e., the slope of $u_n^p - u_\tau^p$ curve). The dilatancy parameters are provided in Table 2.

Table 2: Dilatancy-related parameters for the interface [8]

Parameter	$\tan\psi_0$	$\tan\psi_r$	σ_u (MPa)	δ
Value	0.35	0.001	2.0	0.15

The numerical-experimental comparisons in terms of dilatancy effects are given in Figure 3. The direct shear tests were conducted at three compressive stress levels. Obviously, the dilatancy effects are restricted under a higher compressive stress level and larger shear displacement. In the FE model, the dilatancy effects can be negligible when the absolute value of applied compressive stress $|\sigma_c| > \sigma_u = 2.0 \text{ MPa}$; accordingly, zero slope can be observed in the FE simulation results for the case $|\sigma_c| = 4.31 \text{ MPa}$. It can be observed from Figure 3 that the experimental results can be well reproduced with reasonable material parameters calibrated.

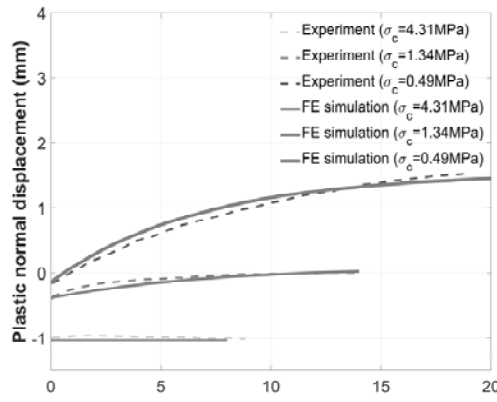


Figure 3: Comparison between numerical and experimental results for the dilatancy curve $u_n^p - u_\tau^p$ at different compressive stress levels

Unreinforced masonry (URM) wall under in-plane (IP) loading

The two URM walls considered in this study were designed to be identical, which were experimentally investigated at Eindhoven University of Technology [9]. The wall dimension is: height=1000mm, width=990mm, and thickness=100mm. The wall's top and bottom courses were

clamped in steel beams, and the wall was tested to failure subjected to a monotonically increasing horizontal load after an initial pre-compression $p_c=0.3\text{MPa}$. Elastic behavior is considered for the unit with the interface element inserted at the middle position, acting as a potential unit crack path. Only tension-shear failure surface is activated in the potential unit crack. For the mortar interface, the material properties are available in the experimental report with a negligible dilatancy effect [9] (i.e., $\tan\psi_0=\tan\psi_r=0$). The material parameters are summarized in Table 3.

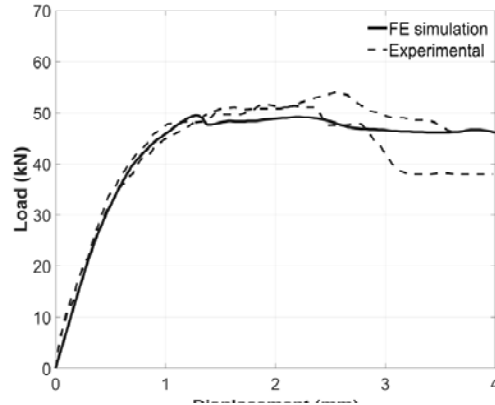


Figure 4: Load-displacement comparison between FE simulation and experiment

Figure 4 shows the simulated global behavior in terms of the load-displacement curve. Although a slight difference can be observed, the FE-predicted load-displacement curves agree relatively well with the experimental results regarding initial stiffness, peak strength, and post-peak behavior.

Table 3: Material parameters for the URM wall J4D

		Parameters	Mortar joints	Unit crack
Elastic		k_{nm} (N/mm ³)	82	1000
		k_{ss} (N/mm ³)	36	1000
		k_{tt} (N/mm ³)	36	1000
Plastic	Tension	f_t (MPa)	0.25	2
		G_I (N/mm)	0.018	0.008
	Shear	c_0 (MPa)	0.35	2.8
		C_{q0}	$100c_0$	$100c_0$
		G_{II}^0 (N/mm)	0.125	0.05
		a	-0.13	-0.2
		$\tan\phi_0$	0.75	1
		$\tan\phi_r$	0.75	1
	Compression	$\text{Tan}\theta$	0.045	
		$\bar{\sigma}_i$ (MPa)	3.5	
		$\bar{\sigma}_p$ (MPa)	10.5	
		$\bar{\sigma}_m$ (MPa)	5.25	
		$\bar{\sigma}_r$ (MPa)	1.5	
κ_p (mm)		0.09		
	κ_m (mm)	0.49		

Figure 5 shows the failure crack pattern in the FE model and experiment. The crack propagation starts from horizontal cracking developed at the bottom and top of the wall, then to the stepped cracking at the center of the wall, and finally to the diagonal crack pattern. The FE simulation result also matches well with the experimental one regarding the local behavior.

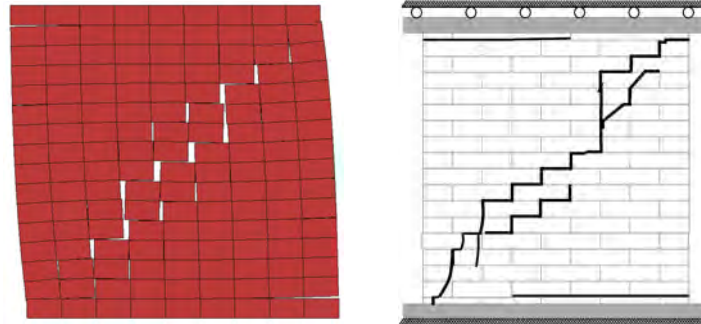


Figure 5: Failure crack pattern for J4D: (a) FE simulation; (b) Experiment

CONCLUSION

A new multi-yield surface model for the interface element was proposed for the finite element analysis of masonry structures. The proposed interface model was formulated and implemented in the general finite element package Abaqus. An error-based auto-adaptive sub-stepping algorithm was used in the fully implicit Backward Euler integration procedure. The variation of dilatancy effect and fracture energy were considered. The interface model was validated by two experimental tests: unit-mortar-unit assemblages and a URM wall. The numerical-experiment comparison results showed that the proposed interface model can be used in the finite element analysis to further explore the complex mechanical behavior of masonry structures.

ACKNOWLEDGEMENTS

The authors would like to acknowledge the financial support provided by the Natural Sciences and Engineering Research Council (NSERC) in Canada through the Collaborative Research and Development (CRD) Grants (CRDPJ 528050-18).

REFERENCES

- [1] Lourenço PB. Computational strategies for masonry structures [Ph.D thesis]. Delft University of Technology, 1996.
- [2] van Zijl GPAG. Modeling Masonry Shear-Compression: Role of Dilatancy Highlighted. *J Eng Mech* 2004;130:1289–96.
- [3] Nazir S, Dhanasekar M. A non-linear interface element model for thin layer high adhesive mortared masonry. *Comput Struct* 2014;144:23–39.
- [4] Pluijm R van der. Out-of-Plane Bending of Masonry: Behaviour and Strength. 1999.
- [5] Gupta A, Krishnan UM, Chowdhury R, Chakrabarti A. An auto-adaptive sub-stepping algorithm for phase-field modeling of brittle fracture. *Theor Appl Fract Mech* 2020;108:102622.

- [6] Simo JC, Kennedy JG, Govindjee S. Non - smooth multisurface plasticity and viscoplasticity. Loading/unloading conditions and numerical algorithms. *Int J Numer Methods Eng* 1988;26:2161-85.
- [7] Abaqus 2017. *Analysis User's Manual*. 2017.
- [8] Atkinson RH, Amadei BP, Saeb S, Sture S. Response of masonry bed joints in direct shear. *J Struct Eng* 1989;115:2276-96.
- [9] Raijmakers TMJ. Deformation controlled tests in masonry shear walls: report B-92-1156. 1992.